Nanoscale

PAPER

View Article Online
View Journal | View Issue

Cite this: *Nanoscale*, 2015, **7**, 10059

Hollow silica sphere colloidal crystals: insights into calcination dependent thermal transport†

P. Ruckdeschel,[a] T. W. Kemnitzer,[b] F. A. Nutz,[a] J. Senker[b] and M. Retsch*[a]

Colloidal crystals consisting of monodisperse hollow silica spheres represent a well-defined porous material class, which features a range of interesting optical, mechanical, and thermal properties. These hierarchically structured materials comprise micropores within the silica network, which are confined to a thin shell (tens of nanometers) of a hollow sphere (hundreds of nanometers). Using simple calcination steps, we markedly change the internal microstructure, which we investigate by a multitude of characterization techniques, while the meso- and macrostructure remains constant. Most importantly the rearrangement of the silica condensation network leads to a reduction in the total surface area and loss of micropores as demonstrated by N_2 sorption and hyperpolarized ^{129}Xe NMR studies. Spin-lattice relaxation shows a drastic increase of the rigidity of the amorphous network. These microstructural changes significantly influence the thermal conductivity through such a porous silica material. We demonstrate a remarkably low thermal conductivity of only 71 mW m^{-1} K^{-1} for a material of a comparatively high density of 1.04 kg m^{-3} at 500 °C calcination temperature. This thermal conductivity increases up to 141 mW m^{-1} K^{-1} at the highest calcination temperature of 950 °C. The great strength of hollow silica sphere colloidal crystals lies in their hierarchical structure control, which allows further investigation of how the internal microstructure and the interfacial contact points affect the transport of heat.

Received 20th January 2015,
Accepted 27th April 2015

DOI: 10.1039/c5nr00435g

www.rsc.org/nanoscale

Introduction

Thermal insulation is an important and indispensable part of current strategies to lower our total energy consumption worldwide. For insulation applications most commonly highly porous materials are being used such as foams or mineral wool.[1] These materials feature thermal conductivities between 30 and 40 mW m^{-1} K^{-1} due to their combination of an amorphous matrix intercalated by a high volume fraction of air, both being poor heat conductors. Nevertheless, fairly thick layers (tens of cm) of these classic materials are necessary to achieve satisfactorily low values of the overall thermal transmittance for their application in structures and buildings.

Another well investigated class of materials is silica aerogels.[2–4] Quite similar to polymeric foams, they comprise an amorphous skeleton and a particularly low density. The network is composed of amorphous silica, which is massively nanostructured by the presence of micro-, meso-, and macropores. Aerogels feature one of the lowest reported thermal conductivities of all material classes and can reach below 20 mW m^{-1} K^{-1}. They can therefore be considered super-insulation materials, which could make their way into widespread applications.[5] From a scientific point of view the total thermal conductivity κ of such an aerogel material is complex as it is influenced by four individual contributions.

$$\kappa_{\text{total}} = \kappa_{\text{solid conduction}} + \kappa_{\text{gas}} + \kappa_{\text{radiation}} + \kappa_{\text{convection}} \quad (1)$$

These individual contributions depend critically on the actual porosity and microstructure of the respective aerogel material. Details can be found in the literature,[1,5–9] whereas we only want to give a short overview here. Convection is typically negligible due to the small pore sizes, which are present in aerogels. κ_{gas} greatly depends on the type of gas used to fill the free volume, which can take up to 99% in aerogels. The pressure of the atmosphere determines this contribution, which is completely suppressed in a vacuum. The dependence on the pressure of the atmosphere is expressed by the Knudsen formalism, which relates the mean free path of the gas molecule to the domain size of the pores, based on kinetic theory.[10,11] $\kappa_{\text{radiation}}$ depends on the temperature difference between the two surfaces of the aerogel monolith, the ambient temperature and the emissivity κ of these interfaces, which can

[a]University of Bayreuth, Physical Chemistry 1 – Polymer Systems, Universitaetsstr. 30, 95447 Bayreuth, Germany. E-mail: markus.retsch@uni-bayreuth.de
[b]University of Bayreuth, Inorganic Chemistry 3, Universitaetsstr. 30, 95447 Bayreuth, Germany

†Electronic supplementary information (ESI) available. See DOI: 10.1039/c5nr00435g

be calculated using the Stefan–Boltzmann equation.[8,12] Assuming that all pores are connected in series by air gaps leads to a dependence on the pore size. Ideally, the contribution of thermal radiation becomes less with decreasing pore size. However, it has to be noted that pores much smaller than the wavelength of the IR radiation may be less effective in reducing this contribution.[1] Furthermore, coupling between radiation and solid conduction can significantly alter the temperature distribution between the two material surfaces, which can result in higher contributions from thermal radiation.[8] Ways to suppress radiation contributions are given by the introduction of absorbing or reflecting moieties.[9,12] $\kappa_{\text{solid conduction}}$ increases with increasing density. Thermal energy is transported along the amorphous silica network by vibrational modes, which can be classified into propagons (propagating and delocalized) and diffusons (nonpropagating and delocalized).[13,14] The third class of vibrational modes, locons (nonpropagating and localized), do not contribute significantly to thermal transport.[15] Whereas a full atomistic understanding of thermal transport through amorphous silica still has to be established, Larkin *et al.* calculated that the contribution from propagating modes amounts to only ~6% of the total thermal conductivity.[15] At the same time the thermal conductivity accumulation function saturates at a mean free path (MFP) of only 10 nm for amorphous SiO_2, which is reflected in an independence of the thermal conductivity from the layer thickness of the amorphous film.[15] These calculations fit well to experimental data from Regner *et al.*, who used broadband frequency domain thermoreflectance to measure the thermal conductivity accumulation function.[16] More complicated systems, such as silica films with microporosity, however, are still elusive to be described by molecular dynamics or finite element simulations as shown by Coquil *et al.*[17] Experimentally, no influence of the symmetry of the micropores was observed using the 3ω technique.[18] Considering the situation of silica aerogels, one has to further take the influence of thermal transport across interfaces into account, as the thermal energy has to diffuse through the individual nanoclusters.[19]

Even though much progress has been made to fabricate silica aerogels over the last few decades, the mandatory supercritical drying step still presents an obstacle to their widespread use and implementation in other technologies.[2,3,20] A work-around to this delicate processing step is possible by the use of hollow spheres, which can be used in a vast range of applications by themselves.[21] In particular hollow silica nanoparticles (HSNP) can be conveniently fabricated by a template polystyrene particle process and thereby allow access to monodisperse particles with adjustable size and porosity.[22] Monodisperse hollow silica particles feature intriguing properties such as a coloration effect caused by Mie resonance,[23] as well as rich mechanical properties, both as single spheres[22,24] and in an ensemble structure.[25,26] Such particles can be processed by standard dispersion technologies into various nano- and mesostructured films, or they can be turned into dry nanoparticle powders. Whereas the record low densities of aerogels are hard to achieve in order to retain the structural integrity of the hollow spheres, they yield well-defined porous materials, which comprise a hierarchy of length scales. The silica shell can be as thin as 10 nm with an additional microporosity in the silica network. The size of the particles typically ranges from 100 nm up to several μm, depending on the size of the templating sphere. All these can be adjusted on a single particle level, with an additional length scale and symmetry to be added upon assembling those colloidal building blocks, which can result in crystalline or amorphous meso- or macrostructures.

Despite their structural complexity and ease of fabrication, only a little is known to date on the thermal conductivity of ensembles of hollow silica spheres.[27–30] Previous studies showed indeed the low thermal conductivity of hollow silica powders in the range from 20 to 33 mW m^{-1} K^{-1}. However, using the transient hot disk, the hotwire, or the 3ω technique, the authors did not specify details of the measurement parameters nor of the micro- or mesostructure of the hollow sphere powder under consideration. In such granular materials the contact points and adhesion between the spheres are of particular importance for the overall transport process along the silica network, as has been appreciated in previous studies, too.[19,28] Here, we want to fully capitalize on the well-defined structure of colloidal crystals consisting of hollow spheres. Our aim is not to demonstrate a record breaking ultralow thermal conductivity, but we want to introduce this material class as a platform to study the fundamentals of thermal transport in amorphous particle based materials. Specifically, we want to answer the question of how the internal microstructure of silica and the mutual contact points determine the thermal conductivity of the particle ensemble. We therefore measure specifically the thermal transport processes through the solid silica network by the laser flash technique.

Results and discussion

As outlined in the Experimental section we utilize hollow spheres of 316 nm diameter and 44 nm shell thickness. These are prepared by coating a polystyrene (PS) template with silica and ensuing calcination of the core/shell structure. Decomposition of the PS core sets in at about 300 °C. For quantitative combustion of the PS core, calcination has been carried out at 500 °C for 12 h. Thermal elemental analysis confirmed the complete combustion process by a lack of carbon in the 500 °C calcined spheres (see ESI Table S1†). This is also confirmed by thermogravimetric analysis (TGA), where a loss of ~2% is observed due to the removal of intercalated water (Fig. S5 in the ESI†). Another 1% of mass is lost up to 950 °C, which can be attributed to the removal of trace amounts of silica condensation products like water. During this core-removal calcination step the outer diameter of the core/shell sphere shrinks by about 2% when transitioning into hollow spheres. Uniformity and monodispersity are most important for a good struc-

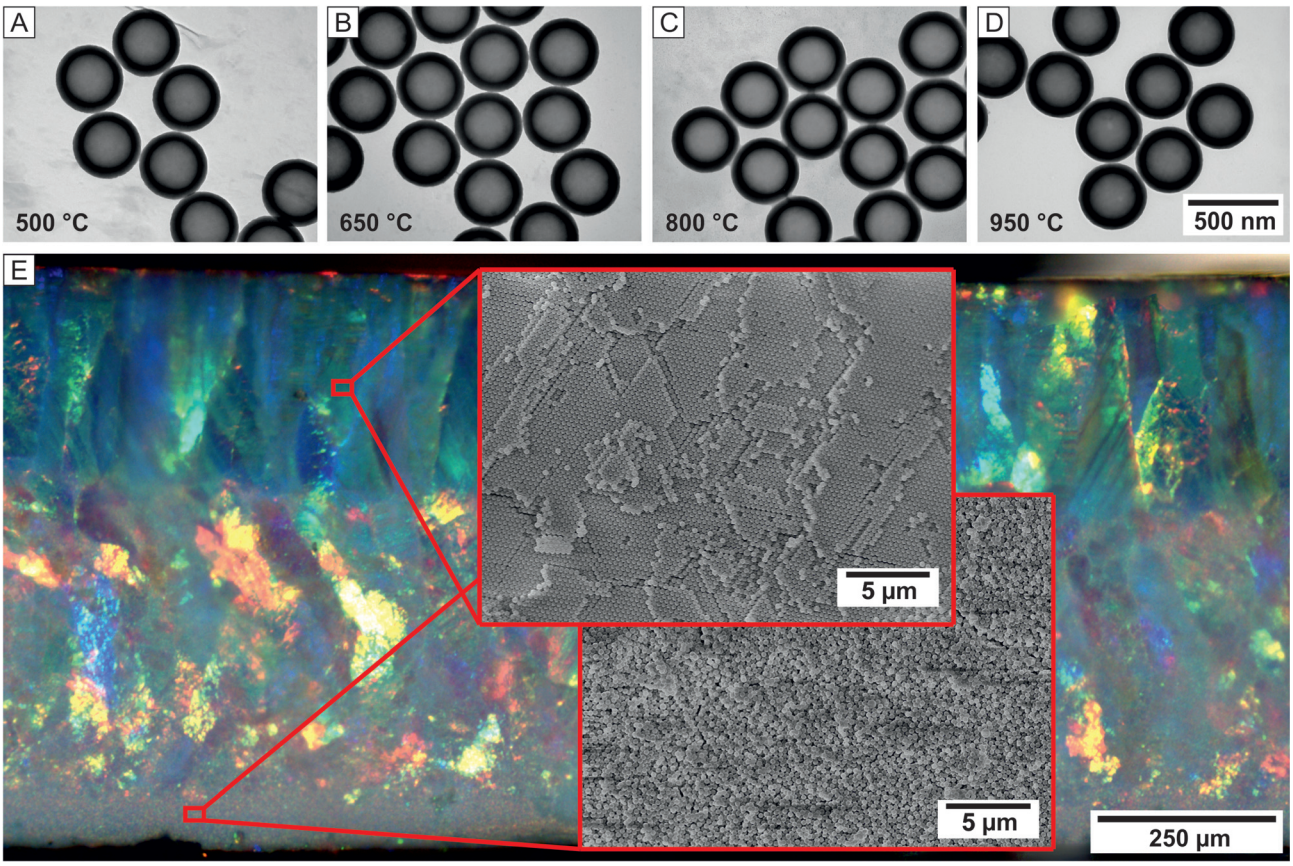

Fig. 1 (A–D) TEM images of hollow silica nanoparticles at different calcination temperatures (500–950 °C). The particle dimensions remain constant for the various calcination temperatures and do not show any clustering. (E) Correlative light and electron microscopy (CLEM) images of a HSNP colloidal crystal calcined at 500 °C. The bright colors are caused by coherent Bragg scattering. Most of the crystal is in a fully crystalline state as confirmed by the scanning electron microscopy (SEM) insets.

tural control of the individual particle, as well as for the assembly into a colloidal crystal, which defines the neighbouring contact points. Transmission electron microscopy (TEM) images demonstrate the size and shape of the hollow spheres (Fig. 1a–d). One can deduce that the spheres remain fully intact during the calcination cycle; they do not feature any cracks or dents. From the projection in the TEM the shell thickness can be measured, which is given by the dark shaded ring that surrounds the hollow core. The surface of the spheres appears smooth (ESI Fig. S1†), and the particles do not form aggregates or clusters. No sinter necks between the spheres or clusters can be seen in the TEM image, but they are rather individually redispersed in ethanol and deposited on the carbon-coated TEM grid. Quite importantly, the hollow spheres demonstrate only a minor shrinkage of their diameter and shell thickness after being subjected to higher calcination temperatures up to 950 °C. As can be seen in Table 1, the diameter slightly shrinks from 316 nm to 310 nm, whereas the shell thickness remains almost constant at 44 nm. In order to further characterize the shape of the hollow spheres, we performed SAXS measurements (ESI Fig. S2a†). A multitude of diffraction orders can be observed, which are fitted using the form factor of a vesicle. The data match well to the TEM measurement and further prove the monodispersity of the hollow spheres.

The functional properties of the hollow spheres only come into play when being assembled into a colloidal superstructure. We therefore used colloidal self-assembly of the core/shell particles as well as hollow spheres calcined at 950 °C, both dispersed in water, in order to fabricate macroscopic monoliths of highly ordered colloidal crystals. Simple drying in PTFE beakers for several days turned out to be the most efficient way to obtain suitable monoliths.

Fig. 1e shows the side-view on a representative colloidal crystal after self-assembly from core/shell particles and calcination at 500 °C. The thicknesses of colloidal crystals under investigation here ranged from about 390 µm to 875 µm. Due to the particle size of 316 nm diameter the crystallinity of the colloidal crystal can be assessed by its bright opalescent colors. Different lattice orientations are exposed to the surface, which causes a multitude of colors observable in Fig. 1e. We used correlative light and electron microscopy to determine the crystallinity of the hollow sphere monolith. Two specific areas are highlighted in Fig. 1e. The top area

Table 1 Summary of data received from TEM, He pycnometry and N_2 sorption measurements

	TEM[a]		Density	N_2 sorption measurement[c]			
	d [nm]	t [nm]	ρ (CC)[b] [g cm^{-3}]	S_{BET} [m^2 g^{-1}]	$V_{tot,DFT}$ [cm^3 g^{-1}]	$V_{mic,DFT}$ [cm^3 g^{-1}]	V_{mic}/V_{tot} [%]
HS-500	316 ± 4	44 ± 2	1.044	113.9	0.101	0.028	27.4
HS-650	316 ± 4	43 ± 2	1.037	70.0	0.087	0.010	11.0
HS-800	314 ± 6	44 ± 2	1.050	26.3	0.053	0	0
HS-950	310 ± 4	43 ± 2	1.047	19.7	0.045	0	0

[a] d: diameter, t: shell thickness. [b] Density of the colloidal crystal (CC) calculated using the density of the silica shell obtained from helium pycnometry measurements ($\rho(SiO_2$, shell) = 2.27 g cm^{-3}) and assuming an fcc packing fraction of 0.74. [c] S_{BET}: surface area calculated by using the BET method, $V_{tot,DFT}$: total pore volume determined by using the NLDFT model on silica at 77 K, $V_{mic,DFT}$: pore volume for pores with diameters smaller than 2 nm determined by using the NLDFT model on silica at 77 K.

with greenish opalescence constitutes highly ordered, hexagonal periodicities of the hollow spheres. Such areas expand over a large range as single crystalline domains. As can be inferred by the opalescence, the vast majority of the hollow sphere ensemble is fully crystalline. Only at the very bottom the long-range crystalline order is compromised and the particles appear to be in a jammed state with only small crystallites persisting. Based on this study, we can safely assume that the volume fraction of the particles in the colloidal crystal is close to its ideal value of 74%. This value represents an upper limit, since the amorphous components will slightly lower the real volume fraction. In combination with He pycnometry measurements, which resulted in a density of the silica shells – independent of the calcination temperature – of $\rho_{silica,\ shell}$ = 2.27 g cm^{-3}, we can calculate the effective density of the hollow sphere colloidal crystal. For the hollow spheres under consideration here, we obtain $\rho_{HSNP,\ CC} \approx 1.04$ g cm^{-3} (see Table 1).

Whereas the geometric structure of a colloidal crystal consisting of hollow sphere particles remains almost identical for a large range of calcination temperatures, the internal structure changes quite considerably. Therefore any changes to the thermal conductivity can be linked to the microstructure of the silica shell. This internal structure is characterized by a certain surface area, a porosity defined by micropores, as well as the degree of condensation and the rigidity of the SiO_x network. We used N_2 adsorption isotherms as well as hyperpolarized ^{129}Xe NMR spectroscopy to characterize the surface area and the pore size distribution within the silica shell (Fig. 2). We find that the particles being calcined at 500 °C feature the largest BET surface area of about 114 m^2 g^{-1}. Please note that we did not add any structure directing agents to the Stöber process to specifically increase the surface area or to template certain types or symmetries of micropores.[18] The isotherms do not show any pronounced hystereses and point towards the presence of micropores (steep slope at low p/p_0), mesopores of small diameter (shallow slope at intermediate p/p_0), and macropores (Fig. 2a). Upon calcination at higher temperatures, these mixed isotherms change considerably. The surface area gradually decreases, leading to a BET surface area of only 19.7 m^2 g^{-1} for the highest calcination temperature used in this study. Estimating the surface area of a hollow sphere powder of our particles leads to a slightly smaller surface area of 12.6 m^2 g^{-1}, when only the outer interface was accessible. Taking into account some surface roughness of the hollow spheres indicates that most of the silica shells are impassable for N_2 after calcination at 950 °C. The drop in the surface area is accompanied by a loss of the total pore volume (from 0.101 cm^3 g^{-1} to 0.045 cm^3 g^{-1}) and micropore volume (Fig. 2c). In particular no micropore volume can be derived from the N_2 isotherms at calcination temperatures beyond 800 °C any more (Table 1).

The pore size distribution obtained by NLDFT analysis, shown in Fig. 2b, confirms the closure of micropores of about 5–8 Å in radius. Exceeding the information accessible by N_2 sorption, the usage of hyperpolarized ^{129}Xe NMR reveals more details of the internal structure at the highest calcination temperatures (Fig. 2d). Two trends become obvious in the ^{129}Xe spectra. Considering the same measurement temperatures the signal intensity decreases with increasing calcination temperatures. This confirms the gradual closure of the micropores with increasing calcination temperature. From the limiting shifts $\delta(^{129}Xe) \sim 57$ ppm and 105 ppm determined at room temperature for the sample calcined at 500 °C two microporous cavities with diameters of 7 Å and 11 Å, were derived using the Fraissard model for cylindrical pore geometry (compare ESI Table S2†).[31] This is in good agreement with the pore radius distribution calculated from the N_2 sorption measurements. For all calcination temperatures the ^{129}Xe signals shift high-field with increasing measurement temperature due to the reducing Xe–Xe interactions as the pores gradually empty. Although for higher calcination temperatures the limiting shift could not be determined experimentally at room temperature due to the decreasing intensity, this trend indicates that even at 800 °C and 950 °C calcination temperatures some microporous cavities remain (Fig. 2d). This is in line with the decreasing micropore volume derived from the sorption data.

The evolution of an asymmetry for the ^{129}Xe gas peak at 0 ppm for all calcination temperatures is in line with filling mesoporous cavities at lower measurement temperatures (Fig. S3a†).[32] This can be rationalized by the geometry of the

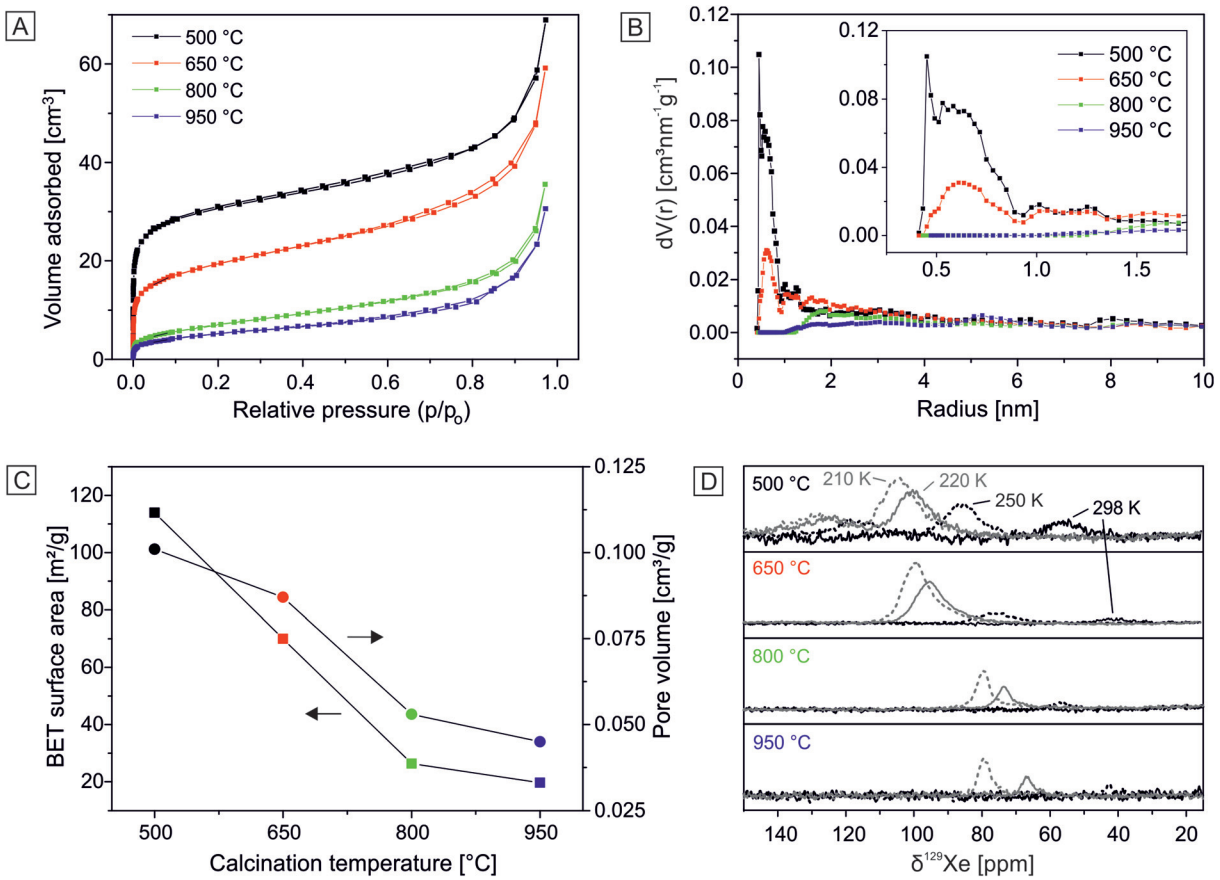

Fig. 2 Internal structural characterization of hollow silica spheres in dependence of the calcination temperature: (A) Nitrogen adsorption and desorption isotherms measured at 77 K allow the determination of pore volume and surface area. (B) Pore radius distributions, calculated by applying the NLDFT silica kernel based on a cylindrical pore model, indicate closure of the micropores at higher calcination temperatures. (C) BET surface area (squares) and pore volume (dots) as a function of calcination temperature. (D) ^{129}Xe NMR spectra of hyperpolarized xenon in silica hollow spheres as a function of the sample temperature. Even for the highest calcination temperatures a small amount of micropores is still present in the silica shell.

contact points between the adjacent spheres, which can be considered to be conical pores.

Despite the rearrangement, which happens during the high temperature calcination, the SiO_2 network remains in its fully amorphous state. Powder XRD measurements on all four samples do not show any onset of crystallization (ESI Fig. S2b†). Only broad halos, indicating the glassy state of the SiO_2 network, can be observed.

As demonstrated by Zhang *et al.*, silica networks obtained by the Stöber method predominantly consist of Si atoms, which are connected to three (Q^3) or four (Q^4) neighbouring –O–Si– units. The ratio between Q^3 and Q^4 changes with increasing calcination temperature and ultimately leads to a fully condensed SiO_2 network.[24] We also characterized our hollow silica spheres by solid state MAS ^{29}Si NMR. The spectrum of a calcined sample at 500 °C is given in Fig. 3a (the other spectra are shown in the ESI in Fig. S4†). By deconvoluting the individual contributions from Q^3 and Q^4 using a pseudo-Voigt function, we determined the ratio of Q^4 to be already 88% in the 500 °C sample. This ratio increases up to 94% for the case of 950 °C calcination (ESI Table S2†). It demonstrates a certain degree of rearrangement within the SiO_2 network upon exposure to higher temperatures, yet the size of the particles stays constant. More prominent are the concomitant changes in the spin-lattice relaxation time T_1 (Fig. 3b). We measured an increase from about 33 s for the hollow spheres calcined at 500 °C up to 6400 s for the highest calcination temperature. This clearly hints towards an increase of the rigidity of the still amorphous silica network, which may also improve the thermal transport capabilities. We confirmed that T_1 is almost independent of the amount of adsorbed water. This was observed at low calcination temperatures by ^{1}H NMR studies (ESI Fig. S3b†). Whereas the broad water peak vanishes in the ^{1}H NMR after the drying procedure, the T_1 changes from 33 s to 20 s for the untreated and predried samples calcined at 500 °C (compare Table S2 in the ESI†).

All these changes to the internal structure (surface area reduction, closure of micropores, increase of Q^4 content and increase of rigidity) happen simultaneously during calcination and are summarized in Fig. 4.

Besides the marked changes to the internal structure of the silica shell, the contact area between the adjacent spheres can

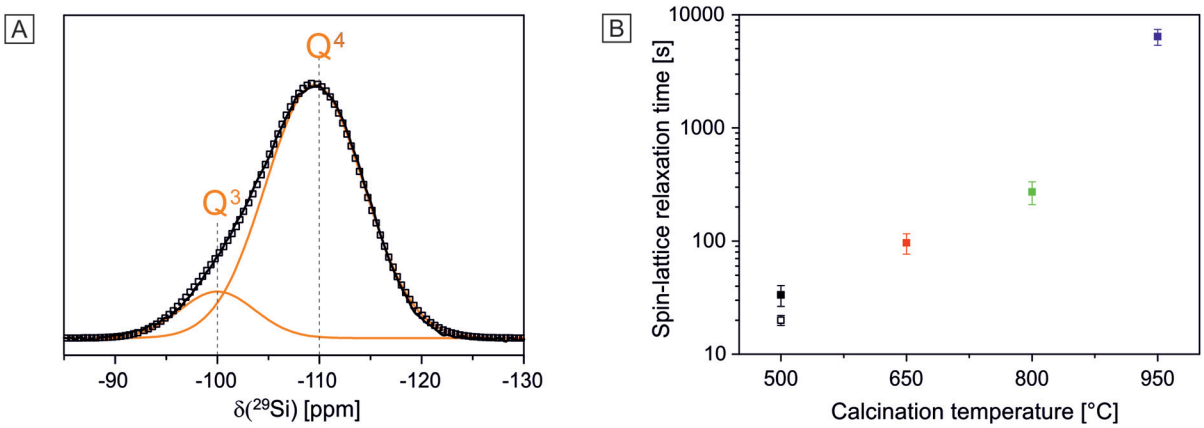

Fig. 3 Internal structural characterization of hollow silica spheres. (A) Deconvoluted projection of the ^{29}Si spectrum of HSNP calcined at 500 °C; measured signal (black line), cumulative fit (open squares), simulated signals (orange lines), (B) Spin-lattice relaxation time of silica hollow spheres calcined at different temperatures. The closed symbols represent untreated and the open symbol pre-dried powder to remove water residues.

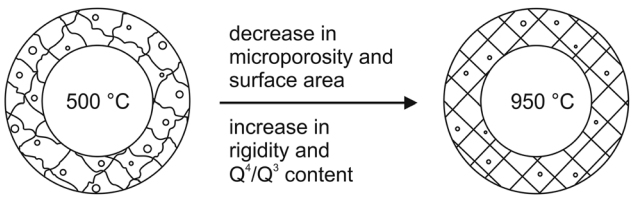

Fig. 4 Schematic representation of the internal structural changes upon high temperature calcination.

also be largely influenced by higher calcination temperatures. Colloidal crystals, with a hexagonally close packed structure, feature twelve neighbouring spheres around each particle. In a vacuum the thermal energy through such a colloidal structure can only be transported along the SiO_2 network. Therefore the contact points between the adjacent spheres play a paramount role. Concomitantly to the changes of the internal structures, the degree of condensation between two spheres at the contact area is also likely to increase. These subtle changes, however, cannot be characterized or quantified, due to the small amount of atoms involved. From the SEM images (ESI Fig. S1†) we can merely deduce that the contact points between the spheres increase slightly from (46 ± 13) nm at 500 °C to (64 ± 12) nm at 950 °C. In order to separate these two contributions to thermal transport (internal structural changes and contact area changes), we conducted two separate sets of experiments. In the first one, we assembled a colloidal crystal from core/shell particles. After calcination at 500 °C we obtained the hollow sphere colloidal crystal. This monolith was repeatedly characterized after calcination at different temperatures of 650 °C, 800 °C and 950 °C for 12 hours (solid symbols in Fig. 6b). This experiment is sensitive to both types of internal and interfacial changes at the same time. In the second experiment, we self-assembled hollow silica spheres from an aqueous dispersion, which have beforehand been subjected to calcination at 950 °C. These hollow spheres featured a surface area of roughly 20 m^2 g^{-1}, similar to the 950 °C calcined particles of the first experiment, indicating a comparable internal structure. Analogously to the samples of the first experiments (compare Fig. 1e) a colloidal crystal with large monocrystalline areas was obtained (see ESI Fig. S8†). The degree of crystallinity decreases from top to bottom with some amorphous areas at the lower end. The samples of this set of experiment are only sensitive to changes in the interfacial contact areas, since the internal structure already resembles a highly condensed network with a small surface area and closed micropores. Annealing of this colloidal crystal at elevated temperatures will consequently only strengthen the interfacial contact points, but will leave the internal structure unaffected. By these two sets of experiments (calcined and annealed colloidal crystals) we can differentiate between contributions made from the internal structure and interfacial changes.

We performed laser flash analysis (LFA) on both types of hollow sphere colloidal crystals. The principle of measurement is depicted in Fig. S6b in the ESI.† A typical measurement along with its fit is provided in Fig. 5a (further LFA measurements are shown in Fig. S7 in the ESI† along with a description of the radiation fit model). At first we investigated the temperature-dependent thermal diffusivity of a hollow sphere colloidal crystal from room temperature up to 200 °C (note that this sample has been calcined at 500 °C, and was stored under ambient laboratory conditions). The heating and cooling cycles are identical after the initial pre-conditioning as outlined in the Experimental section (ESI Fig. S7b†). The pre-conditioning removes adsorbed water in the silica shell (compare ^{1}H NMR of HSNP calcined at 500 °C in Fig. S3b in the ESI†). We conducted our experiments on at least three distinct samples of the hollow sphere colloidal crystals, each varying slightly with respect to the overall sample thickness. Fig. 5b shows only a small increase in thermal diffusivity

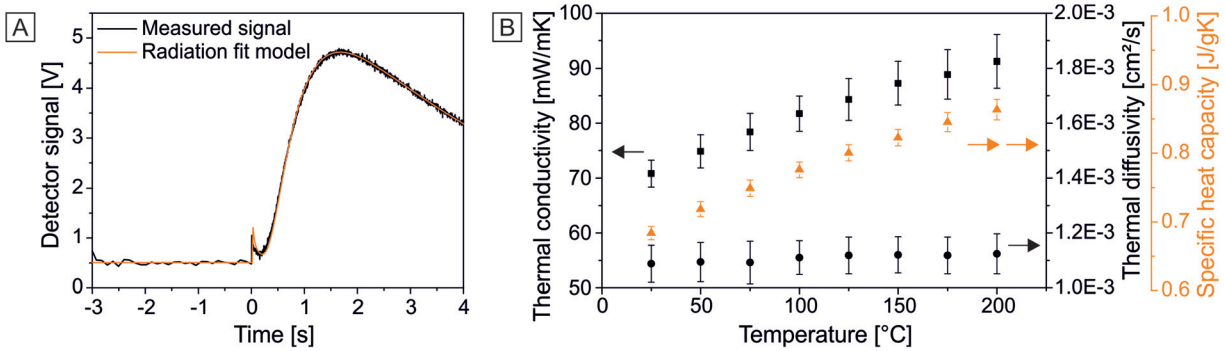

Fig. 5 LFA measurements of HSNP calcined at 500 °C. (A) Measured signal (black line) with the radiation fit model (orange line). (B) Summary of the necessary input parameters (thermal diffusivity – black circles and mean specific heat capacity – orange triangles) to determine the thermal conductivity (black squares).

α along with the specific heat capacity c_p in the temperature range from 25 °C to 200 °C. Using the equation

$$\kappa = \alpha \rho c_p \quad (2)$$

the thermal conductivity κ can be calculated. As demonstrated above, the density ρ of the silica shell and therefore of the hollow sphere colloidal crystal does not change within this temperature range, and stays almost constant up to calcination temperatures of 950 °C. The uncertainty of the density determination is about 9%.

Since we conduct our measurements in a vacuum, we use the c_p obtained from DSC measurements of the silica shell (from compacted hollow spheres). The specific heat capacity shows a monotonic increase in the temperature range of interest, but is hardly influenced by the calcination temperature (see Fig. S5b in the ESI†). We therefore used the same average temperature dependent c_p for all samples under consideration here, which is close to the literature value of quartz glass (c_p = 0.73 J g^{-1} K^{-1}).[33] The standard deviation of the c_p amounts to about 2%. The slightly reduced c_p of our silica shell could be attributed to a small amount of porosity and differences in the network condensation, compared to fused quartz glass reported in the literature. Combining the individual uncertainties of the thermal diffusivity, density, and specific heat, we find that the determination of κ is accurate to within ±5–13% for an individual measurement. Variations from sample to sample during the different calcination steps can be therefore regarded as the main source of error (details are reported in the ESI†: uncertainty analysis of the thermal conductivity determination). We therefore show the average values and standard deviation of at least three independent samples in Fig. 6.

Fig. 6a shows all temperature-dependent thermal conductivities for samples after various calcination temperatures. The thermal conductivity of a 500 °C calcined hollow sphere colloidal crystal consisting of 316 nm diameter and 44 nm shell capsules is very low with κ = 71 mW m^{-1} K^{-1}. The thermal conductivity increases monotonically to a value of κ = 91 mW m^{-1} K^{-1} at 200 °C, which is known for glassy materials at high temperatures.[34,35] It is higher compared to most bulk silica aerogels and previously reported hollow spheres, however, the effective density of the colloidal crystal under investigation here is relatively high with ρ = 1.044 g cm^{-3}. Calcination at elevated temperatures leads to a systematic increase in thermal conductivity, the absolute magnitude doubles at room temperature from κ = 71 mW m^{-1} K^{-1} (calcination at 500 °C) to κ = 140 mW m^{-1} K^{-1} (calcination at 950 °C). In comparison with calcination dependent investigations that have been carried out on silica aerogel samples we attribute this increase not to a loss in methyl groups or increase in density, but solely to microstructural changes, since the density of our silica shell is constant from calcination between 500 °C and 950 °C.[36] This is corroborated by a thermogravimetric analysis of the 500 °C calcined hollow spheres (ESI Fig. S5a†).

In the further discussion we only want to focus on the thermal conductivity at 25 °C. Concomitant with the increase in thermal conductivity at higher calcination temperatures, the standard deviation also increases. This can be understood by small, but random changes from sample to sample during the calcination process. These changes can be the evolution of cracks or line defects, or a change in the adhesion between the neighbouring spheres. As outlined above, the individual spheres remain almost constant in size even at high calcination temperatures. However, within an ensemble of particles these minute changes can accumulate to distinct defects. Such changes are small and we could not observe any structural changes by optical microscopy or SEM (see Fig. S1 in the ESI†). Since the samples of annealed colloidal crystals also demonstrate the same amount of increase in data scattering, the evolution of the mutual contact points seems to be the major source for this scattering. In addition, an increase in thermal conductivity can lead to higher losses into the sample holder during the LFA measurement. This in turn can reduce the accuracy of the radiation fit model.

Despite some scatter in the data, the unambiguous trend of an increase in thermal conductivity can be inferred from the inset of Fig. 6b (closed symbols). Due to the well-defined struc-

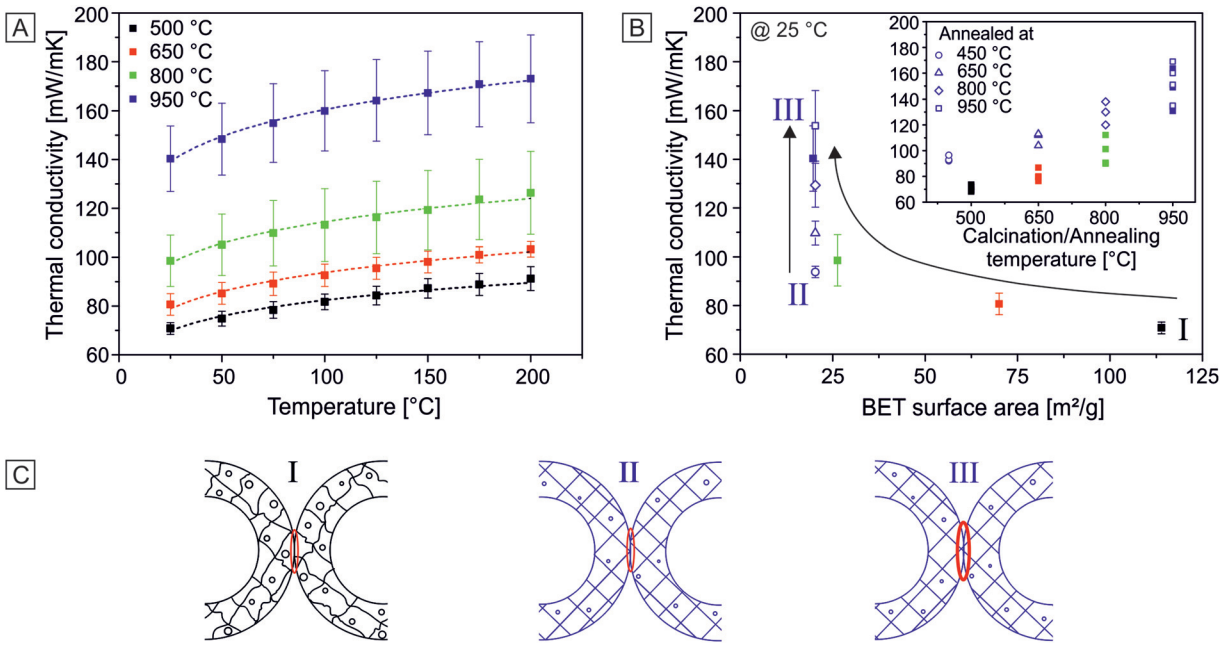

Fig. 6 Thermal conductivity of calcined (closed symbols) and annealed HSNP colloidal crystals (open symbols). (A) Thermal conductivity of HSNP monoliths calcined at different temperatures (500–950 °C) as a function of the measurement temperature. The dashed lines represent $\kappa \sim T^{x}$. (B) BET surface area and calcination temperature (inset) as a function of the thermal conductivity at 25 °C measurement temperature. (C) Schematic representation of the internal structural changes and the increase in interfacial adhesion within a colloidal crystal ensemble.

ture, we can now relate this apparent increase to microstructural changes in the SiO_2 network. We therefore plot the same data against the BET surface area, which changes sensitively with the calcination temperature as shown above. The reduction in the surface area by a factor of almost six leads to a doubling of the thermal conductivity (Fig. 6b solid symbols). However, this change is accompanied by the closure of micropores, a small increase in Q^4 Si atoms (ESI Fig. S7c†), a large increase in spin-lattice relaxation time, and most importantly an increase of the interfacial adhesion between the spheres. These changes are schematically shown in Fig. 6c. The relative area (based on the total particle surface) involved in interfacial contact points, increases with higher calcination temperatures from ~6% at 500 °C to ~13% at 950 °C (see Fig. S1†). This can additionally contribute to an improved thermal transport between the individual particles due to less constriction resistance. We therefore also investigated the thermal transport properties of annealed colloidal crystals as outlined above. Fig. S7d in the ESI† shows all temperature-dependent measurements of the annealed samples, similar to Fig. 6a. The data from the 450 °C up to 950 °C annealed colloidal crystals are shown with open symbols in Fig. 6b and correspond to a transition from Fig. 6c II to III. The BET surface area of the hollow spheres and therefore of the colloidal crystal has already been reduced to only 20.3 $m^2\ g^{-1}$ prior to the colloidal crystal formation. This surface area does not change with increasing annealing temperatures any more, as the SiO_2 network has already been brought into its highly condensed form. Consequently, the data lie on a straight vertical line in Fig. 6b (open symbols). One recognizes that the loss of micropores and increase in the rigidity of the silica network (*i.e.* the T_1 relaxation) lead to a distinct increase in thermal conductivity from κ = 71 mW m^{-1} K^{-1} to κ = 92 mW m^{-1} K^{-1} – while the interfacial contact between the spheres can be regarded similar to the 500 °C calcined crystal (closed black square). In contrast it also demonstrates the large influence of interfacial adhesion as the thermal conductivity is drastically reduced compared to the fully annealed case (open blue circles, κ = 154 mW m^{-1} K^{-1}). Annealing at 650 °C, 800 °C, and ultimately 950 °C strengthens the covalent linkage at the contact points of the adjacent spheres, but will not change the internal structure any further (transition from Fig. 6c II to III). This increase in adhesion is reflected in a marked increase in thermal conductivity of the annealed hollow sphere monoliths (open symbols) from κ = 94 mW m^{-1} K^{-1} (500 °C) to κ = 110 mW m^{-1} K^{-1} (650 °C), κ = 129 mW m^{-1} K^{-1} (800 °C), and κ = 154 mW m^{-1} K^{-1} (950 °C). The final value of 154 mW m^{-1} K^{-1} is a little higher, compared to the calcined colloidal crystal (κ = 140 mW m^{-1} K^{-1}). This could be due to the absence of shrinkage in the case of annealing in contrast to calcination where the spheres shrink slightly from 316 nm to 310 nm (compare Table 1). This could be reflected in less defects and broken contact points.

What do we learn about the transport of thermal energy through such an amorphous, nanostructured silica material? The transport of thermal energy in this amorphous material is influenced by two distinct contributions: the microstructure of the "bulk" silica network (the thickness is only 44 nm) and the

interfacial contact between the adjacent spheres. The influence of the bulk silica network can be seen by the difference between the colloidal particles calcined after (Fig. 6b solid symbols) and before (Fig. 6b open symbols) the assembly process. Assuming a comparable adhesion between the silica spheres at the respective calcination and annealing temperatures, the annealed colloidal crystals always demonstrate a higher thermal conductivity. Apparently, the minimum amount of micropores in combination with a higher degree of Q^4 atoms and a smaller BET surface area leads to less scattering of delocalized modes at point defects or interfaces. Furthermore, the increase in spin-lattice relaxation time can be interpreted as a measure to increase the coherence length of the vibrational modes in the amorphous network, which will result in an increased thermal transport. A similar effect has been reported for amorphous polymers, where weak van der Waals bonds have been replaced by stronger hydrogen bonds.[37] Accordingly, we also observe a decrease in the temperature dependence from $\kappa \sim T^{0.5}$ for 500 °C calcination to $\kappa \sim T^{0.4}$ for 950 °C calcination (determined by a linear fit to a double-log plot of the κ *vs.* T graph). The annealed samples show a $\kappa \sim T^{0.4}$ dependency, which slightly decreases with higher annealing temperatures (see ESI Fig. S7d†). As a reference, fused quartz glass demonstrates a proportionality of $\kappa \sim T^{0.3}$ in the respective temperature range between 0 °C and 200 °C. The temperature dependence of the thermal conductivity can provide insights on how thermal energy is transported. For crystalline materials the temperature-dependent thermal conductivity is known to scale with T^{-1} (at high temperatures) due to phonon–phonon Umklapp scattering.[34,38] For disordered materials the scaling behaviour exhibits typically a positive slope due to an increase in heat capacity and the diffusive thermal conduction of propagons and diffusons. In our amorphous material, we find the expected increase in thermal conductivity with increasing temperatures. This dependency, however, decreases slightly from $T^{0.5}$ to $T^{0.4}$ with increasing calcination temperature. We attribute this decrease to an increased anharmonic coupling between localized modes or between localized and delocalized modes, caused by the microstructural changes during the calcination.[39]

Even more important, particularly when considering the small amount of atoms involved, are the interfacial contact points between the adjacent spheres. Due to the fcc structure, each particle contacts twelve neighbouring particles. For the case of annealed colloidal crystals, the adhesion and the degree of crosslinking between the spheres govern predominantly the thermal transport, since the internal structure is already fully condensed. Whereas we cannot quantify the bonding strength between the hollow silica particles, one can deduce from Fig. 6b (open symbols) that the thermal conductivity can be increased by more than 160%, when strengthening the contact points. Analogously to the calcined samples, a slight increase in the mutual particle contact area may also contribute to the enhanced thermal transport.

The absolute thermal insulation properties of the hollow silica colloidal crystals presented here are less compared to their aerogel analogues; however, they still demonstrate a very low thermal conductivity in particular in the light of the relatively high density ($\rho \approx 1.04$ g cm^{-3}).

Conclusion

Colloidal crystals consisting of hollow silica nanoparticles represent a porous material class, with very well defined nano- and mesostructures. The monodispersity of the constituting building blocks, which comprise two distinct length scales (44 nm shell thickness and 316 nm diameter), translates into highly ordered colloidal crystals. Yet, for thermal transport applications, this material can be considered entirely amorphous, due to the glassy microstructure of the condensed silica network. We employed a range of characterization techniques to determine the structural entities from the nano- to the macroscale. SAXS, electron and optical microscopy showed the structural integrity even after calcination up to 950 °C, whereas NMR, N_2 sorption, and XRD demonstrated significant changes on the nanoscale. These changes result in an increase in thermal conductivity through this porous material. We identified two distinct contributions to this increase in thermal conduction. The first being internal structural changes of the condensed silica network, which are: loss of micropores, loss of BET surface areas, increase in Q^4 Si atoms and increase in spin-lattice relaxation time. The second being an increase in interfacial bonding between the individual spheres. Both result in a higher thermal conductivity of our porous silica material. Even though only a fraction of the total amount of Si and O atoms contribute to interfacial adhesion, the thermal conductivity predominantly depends on it. Combining low adhesion forces and microstructure leads consequently to the lowest thermal conductivity of κ = 71 mW m^{-1} K^{-1} for the system under investigation here. Colloidal crystals of hollow silica nanoparticles not only represent a highly insulating material. The well-defined structure further allows us to thoroughly investigate thermal transport processes in amorphous silica materials. Further research will build upon these concepts and may lead to extremely efficient insulation layers.

Experimental section

Materials

Styrene (≥99%, Aldrich), 2,2′-azobis(2-methylpropionamidine) dihydrochloride (AIBA; 97%, Aldrich), 2-methacryloxy-ethyltrimethylammonium chloride (MTC; 70% solution in water, Polyscience), polyvinylpyrrolidone K30 (PVP; $M_w \sim 55$ kg mol^{-1}, Aldrich), Tetraethyl orthosilicate (TEOS; ≥99%, Aldrich) and ammonium hydroxide solution (30–33% in water, Aldrich) were used as received. Ethanol (EtOH) was used in technical

grade and water was taken from a Millipore Direct Q3UV unit for the entire synthesis and purification steps.

Synthesis of monodisperse hollow silica nanoparticles

The synthesis of monodisperse hollow silica nanoparticles comprises three steps. First monodisperse polystyrene (PS) latex particles were synthesized by emulsifier-free emulsion polymerization. The reaction was carried out in a 500 mL three-neck flask, equipped with a gas inlet and a reflux condenser. Solid chemicals were dissolved in water prior to addition. Firstly 200 mL water, 26 mL styrene, 1.8 g PVP and 100 μL MTC were heated to the reaction temperature of 70 °C at a stirring speed of 850 rpm using a large egg-shaped magnetic stirring bar. After equilibrating for 20 min, 600 mg AIBA initiator, dissolved in 40 mL water, was quickly added to initiate the polymerization. After nucleation, the stirring speed was reduced to 450 rpm and the polymerization was allowed to continue overnight at 70 °C under a slight inert gas flow. In the second step the PS template particles were coated with a silica shell to obtain core/shell particles. The silica coating was achieved by a Stöber condensation process.[40] Therefore 17.5 mL neat PS dispersion (9.14 wt%) were diluted with 122.5 mL ethanol and 9.1 mL ammonium hydroxide solution and stirred at 500 rpm. After stepwise addition of 13 mL TEOS the reaction was stirred overnight at room temperature. The core/shell particles were purified by repeated centrifugation and redispersion in water. In order to prepare hollow spheres, the sample was dried and kept in a furnace (Nabertherm L5/11/P33) at 500 °C, 650 °C, 800 °C or 950 °C in air for 12 h. The hollow spheres could be redispersed in water using mild sonication in a sonication bath.

Colloidal crystal *via* evaporation induced self-assembly of hollow silica nanoparticles

To obtain colloidal crystals a concentrated aqueous solution of core shell particles (~7 wt%) or hollow silica spheres (~5 wt%) was slowly evaporated in a Teflon beaker with a diameter of 2 cm for several days.

Characterization

Transmission electron microscopy (TEM) images were taken on a Zeiss CEM 902 instrument in bright field imaging mode at an acceleration voltage of 80 kV.

Elemental analysis (EA) was performed on a Vario Elementar EL III apparatus.

Nitrogen sorption measurements were carried out on a Quantachrome Autosorb AS-1 pore analyzer at 77 K. Prior to the measurements, all samples were preconditioned in a vacuum at 350 °C for 12 hours. For the analysis, the Quantachrome ASiQ v3.0 software was used. The specific surface areas were calculated using the BET method. Pore volumes and pore size distributions were obtained by applying the nonlocal density functional theory (NLDFT) adsorption branch model for silica materials with cylindrical pore geometry.

Solid-state ^{29}Si NMR and hyperpolarized ^{129}Xe NMR measurements were carried out on a Bruker Avance II spectrometer in combination with a 7.05 T magnet (Oxford) corresponding to a Larmor frequency ω_0 = 59.6 MHz for ^{29}Si and 83.0 MHz for ^{129}Xe equipped with a BVT 3000 VT-Unit (Bruker). ^{29}Si spectra were recorded with single pulse excitation using a 7 mm triple resonance probe at a spinning frequency of 5 kHz. The chemical shifts were referenced to tris(trimethylsilyl)amine (2.4 ppm) relative to tetramethylsilane (TMS). A 90° pulse at a nutation frequency of 38 kHz was used. The repetition times were set to 60 s. The number of scans was adapted such that a sufficient S/N ratio was obtained. Spin-lattice relaxation was measured by using a saturation recovery experiment with a pulse train of 5 90° pulses to ensure complete saturation of the system. The spectra were deconvoluted using a pseudo-Voigt profile by fitting to the least squares. The formula of the applied profile is expressed by

$$I(\delta) = A\left\{\eta\frac{\sqrt{4\ \log\ 2}}{\sqrt{\pi}w}\exp\left[-\frac{4\ \log\ 2}{w^2}(\delta-\delta_0)^2\right] + (1-\eta)\frac{2}{\pi}\frac{w}{\left[4(\delta-\delta_0)\right]^2+w^2}\right\} \quad (3)$$

where A is the amplitude of the peak, δ_0 is its center, η is the weight factor (1: Gaussian function, 0: Lorentzian function) and w is the full width at half maximum (FWHM).

For variable-temperature (VT) hyperpolarized ^{129}Xe NMR measurements a 5 mm wideline double resonance probe (Bruker) was used. The NMR chemical shifts were referenced to the signal of gaseous xenon at 0 ppm. The probe was modified with a 3 mm inner diameter PEEK sample holder to incorporate hyperpolarized ^{129}Xe in continuous flow mode to the sample. The spectra were acquired with single pulse excitation using 52.62 kHz nutation frequency and 32 to 128 transients. The recycle time was set to 1 s and is not dependent on the spin-lattice relaxation but limited by the flow rate and the exchange between hyperpolarized and depolarized ^{129}Xe in the pore.[41] The hyperpolarized ^{129}Xe was generated using a self-built polarizer. A gas mixture of Xe : N_2 : He = 1 : 2 : 97 (vol%) at an overall pressure of 5 bar was irradiated with an 80 W diode laser (Coherent Inc.) at a central frequency of the Rb D_1-line (l = 794.8 nm). The polarized gas was exchanged over the sample with a flow rate of about 200 cm^3 min^{-1}. A polarization of ~5% was reached.

Solid-state ^{1}H NMR measurements were carried out on a Bruker Avance III HD spectrometer using a 14.1 T magnet (Bruker Ascent) corresponding to a Larmor frequency of ω_0 = 600.1 MHz and a 1.3 mm double resonance probe at a spinning frequency of 62.5 kHz. Spectra were acquired with 8 transients at a nutation frequency of 161 kHz and a repeating time of 5 s.

Small-angle X-ray scattering (SAXS) data reported here were measured using the small-angle-X-ray system Double Ganesha AIR (SAXSLAB, Denmark). The X-ray source of this laboratory-based system is a rotating anode (copper, MicroMax 007HF, Rigaku Corporation, Japan) providing a micro-focused beam at l = 0.154 nm. The data were recorded by a position sensitive detector (PILATUS 300 K, Dectris). To cover the range of

scattering vectors between 0.026 and 2.6 nm^{-1} different detector positions were used. The measurement was recorded using a powder of hollow silica nanoparticles between two Kapton foils at room temperature. The scattering curve was evaluated with a vesicle fit in the program SCATTER.[42]

Powder X-ray diffraction (XRD) measurements were performed using a STOE STADI P ($CuK_{\alpha1}$ radiation, transmission geometry) diffractometer equipped with a fast, high resolution silicon strip detector DECTRIS Mythen1 K. The samples were mounted on a flat disk using Scotch® tape. A stepsize of 0.2° and an integration time of 20 s were used.

Differential scanning calorimetry (DSC) measurements were recorded using a Q1000 DSC (TA Instruments). Compressed powders of the hollow spheres (12–15 mg) were scanned in covered aluminium pans under dry nitrogen purge (50 mL min^{-1}) over a temperature range from −50 °C to 200 °C with a heating rate of 10 °C min^{-1}. The heat flow and heat capacity were calibrated using a standard sapphire sample. The received data were evaluated with Universal Analysis 2000 2.5A software.

Thermogravimetric analysis (TGA) was performed with a Mettler Toledo TGA/STDA 851^e Star System at a heating rate of 10 K min^{-1} under air flow. The initial sample weight was 16.8018 mg.

Thermal diffusivity of the colloidal crystals was measured by laser flash analysis (LFA) on a XFA 500 XenonFlash apparatus (Linseis) with an InSb infrared detector. The measurements were taken over a temperature range from 25 to 200 °C in a vacuum. Prior to the measurements the samples were coated with approximately 15 μm of graphite on each side. In order to eliminate any potential contribution from intercalated water inside the SiO_2 network, we pre-heated the samples up to 200 °C for 15 min in a vacuum. The received data were evaluated by the software AproSoft Laser Flash Evaluation v1.06. The thicknesses of the colloidal crystals were determined with a Litematic VL-50 (Mitutoyo).

Correlative light-electron microscopy (CLEM) images were recorded on an Axio Imager.A2 m (Carl Zeiss Microscopy) equipped with a motorized stage and a digital camera AxioCam ICc 1. Using the shuttle & find module the samples were transferred into a scanning electron microscope (SEM) Zeiss Ultraplus mounted on the sample holder KorrMik MAT universal B. SEM images were recorded on pre-defined spots based on the optical light microscopy image using acceleration voltages between 2 and 3 kV and InLens SE detection as well as Everhart–Thornley detection (80/20 or 70/30 ratio).

Acknowledgements

The authors thank Lena Geiling and Nadine Popp for BET, Anna-Maria Dietel for EA, Markus Drechsler for TEM, Martin Dulle for SAXS, Ute Kuhn for DSC, and Beate Förster for CLEM measurements. This project was funded by the Volkswagen foundation. SFB 840 is acknowledged for financial support. P.R. acknowledges support by the Elite Network Bavaria (ENB). M.R. thanks the VCI for financial support.

Notes and references

1 B. P. Jelle, A. Gustavsen and R. Baetens, *J. Build. Phys.*, 2010, **34**, 99–123.
2 A. S. Dorcheh and M. H. Abbasi, *J. Mater. Process. Technol.*, 2008, **199**, 10–26.
3 N. Hüsing and U. Schubert, *Angew. Chem., Int. Ed.*, 1998, **37**, 22–45.
4 S. S. Kistler, *J. Phys. Chem.*, 1931, **36**, 52–64.
5 M. Koebel, A. Rigacci and P. Achard, *J. Sol-Gel Sci. Technol.*, 2012, **63**, 315–339.
6 U. Heinemann, *Int. J. Thermophys.*, 2008, **29**, 735–749.
7 D. M. Smith, A. Maskara and U. Boes, *J. Non-Cryst. Solids*, 1998, **225**, 254–259.
8 U. Heinemann, R. Caps and J. Fricke, *Int. J. Heat Mass Transfer*, 1996, **39**, 2115–2130.
9 L. W. Hrubesh and R. W. Pekala, *J. Mater. Res.*, 1994, **9**, 731–738.
10 M. Knudsen, *Ann. Phys.*, 1911, **339**, 593–656.
11 S. N. Schiffres, K. H. Kim, L. Hu, A. J. H. McGaughey, M. F. Islam and J. A. Malen, *Adv. Funct. Mater.*, 2012, **22**, 5251–5258.
12 X. Lu, M. C. Arduini-Schuster, J. Kuhn, O. Nilsson, J. Fricke and R. W. Pekala, *Science*, 1992, **255**, 971–972.
13 P. Allen and J. Feldman, *Phys. Rev. B: Condens. Matter*, 1993, **48**, 12581–12588.
14 P. B. Allen, J. L. Feldman, J. Fabian and F. Wooten, *Philos. Mag. B*, 2009, **79**, 1715–1731.
15 J. M. Larkin and A. J. H. McGaughey, *Phys. Rev. B: Condens. Matter*, 2014, **89**, 144303.
16 K. T. Regner, D. P. Sellan, Z. Su, C. H. Amon, A. J. H. McGaughey and J. A. Malen, *Nat. Commun.*, 2013, **4**, 1640–1647.
17 T. Coquil, J. Fang and L. Pilon, *Int. J. Heat Mass Transfer*, 2011, **54**, 4540–4548.
18 T. Coquil, E. K. Richman, N. J. Hutchinson, S. H. Tolbert and L. Pilon, *J. Appl. Phys.*, 2009, **106**, 034910.
19 T. G. Desai, *Appl. Phys. Lett.*, 2011, **98**, 193107.
20 J. Fricke and T. Tillotson, *Thin Solid Films*, 1997, **297**, 212–223.
21 M. Chen, C. Ye, S. Zhou and L. Wu, *Adv. Mater.*, 2013, **25**, 5343–5351.
22 L. Zhang, M. D'Acunzi, M. Kappl, G. K. Auernhammer, D. Vollmer, C. M. van Kats and A. van Blaaderen, *Langmuir*, 2009, **25**, 2711–2717.
23 M. Retsch, M. Schmelzeisen, H.-J. Butt and E. L. Thomas, *Nano Lett.*, 2011, **11**, 1389–1394.
24 L. Zhang, M. D'Acunzi, M. Kappl, A. Imhof, A. van Blaaderen, H.-J. Butt, R. Graf and D. Vollmer, *Phys. Chem. Chem. Phys.*, 2010, **12**, 15392.
25 J. Yin, M. Retsch, E. L. Thomas and M. C. Boyce, *Langmuir*, 2012, **28**, 5580–5588.

26 J. Yin, M. Retsch, J.-H. Lee, E. L. Thomas and M. C. Boyce, *Langmuir*, 2011, **27**, 10492–10500.
27 L. I. C. Sandberg, T. Gao, B. P. Jelle and A. Gustavsen, *Adv. Mater. Sci. Eng.*, 2013, **2013**, 1–6.
28 T. Gao, B. P. Jelle, L. I. Sandberg and A. Gustavsen, *ACS Appl. Mater. Interfaces*, 2013, **5**, 761–767.
29 Q. Yue, Y. Li, M. Kong, J. Huang, X. Zhao, J. Liu and R. E. Williford, *J. Mater. Chem.*, 2011, **21**, 12041.
30 Y. Liao, X. Wu, H. Liu and Y. Chen, *Thermochim. Acta*, 2011, **526**, 178–184.
31 J. Demarquay and J. Fraissard, *Chem. Phys. Lett.*, 1987, **136**, 314–318.
32 I. L. Moudrakovski, V. V. Terskikh, C. I. Ratcliffe, J. A. Ripmeester, L.-Q. Wang, Y. Shin and G. J. Exarhos, *J. Phys. Chem. B*, 2002, **106**, 5938–5946.
33 Y. S. Touloukian, *Thermophysical properties of matter: Specific heat/Nonmetallic Solids*, IFI Plenum, New York, 1970.
34 D. G. Cahill and R. O. Pohl, *Annu. Rev. Phys. Chem.*, 1988, **39**, 93–121.
35 D. Cahill and R. Pohl, *Phys. Rev. B: Condens. Matter*, 1987, **35**, 4067–4073.
36 P. E. Hopkins, B. Kaehr, E. S. Piekos, D. Dunphy and C. Jeffrey Brinker, *J. Appl. Phys.*, 2012, **111**, 113532.
37 G. H. Kim, D. Lee, A. Shanker, L. Shao, M. S. Kwon, D. Gidley, J. Kim and K. P. Pipe, *Nat. Mater.*, 2015, **14**, 295–300.
38 C. Kittel, *Einführung in die Festkörperphysik*, Oldenbourg, Wien, 14th edn, 2005.
39 S. Shenogin, A. Bodapati, P. Keblinski and A. J. H. McGaughey, *J. Appl. Phys.*, 2009, **105**, 034906.
40 W. Stöber, A. Fink and E. Bohn, *J. Colloid Interface Sci.*, 1968, **26**, 62–69.
41 B. M. Goodson, *J. Magn. Reson.*, 2002, **155**, 157–216.
42 S. Förster, L. Apostol and W. Bras, *J. Appl. Crystallogr.*, 2010, **43**, 639–646.